



# Finite element thermal stress analysis of solid oxide fuel cell cathode microstructures

Sushrut Vaidya, Jeong-Ho Kim\*

Department of Civil and Environmental Engineering, University of Connecticut, 261 Glenbrook Road, Storrs, CT 06269, USA

## HIGHLIGHTS

- We develop a framework for cathode microstructures in solid oxide fuel cell.
- We develop novel heuristic schemes to derive cathode microstructures.
- Temperature-dependent material properties must be considered.

## ARTICLE INFO

### Article history:

Received 4 July 2012

Received in revised form

17 September 2012

Accepted 15 October 2012

Available online 26 October 2012

### Keywords:

Solid oxide fuel cells

Cathode

Microstructure

Probability of failure

Finite element analysis

## ABSTRACT

Two-dimensional images of solid oxide fuel cell (SOFC) cathode microstructures (50:50 wt.% LSM:YSZ) are used to generate three-dimensional finite element (FE) models. An approximate, heuristic scheme is developed to derive a microstructure of 30:70 wt.% LSM:YSZ composition from the original, real microstructures. The derived model is validated by calculating three-phase boundary (TPB) and phase surface area densities by comparing with data available in the literature. Construction of such derived microstructures will provide insights on the effects of phase compositions on the mechanics of electrode structures. The heuristic scheme is not proposed as a replacement for rigorous approaches such as the random packing model, but rather as a simplified approach for deriving reasonably realistic microstructures of different compositions within a limited range of validity. The models are analyzed using finite elements to estimate thermal stresses and probability of failure using Weibull analysis. The effects of temperature-dependent material properties and phase volume fractions on probability of failure of the cathode are discussed.

Crown Copyright © 2012 Published by Elsevier B.V. All rights reserved.

## 1. Introduction

In recent years, significant research efforts focused on solid oxide fuel cells (SOFCs) have been undertaken in the field of power sources. SOFCs are capable of directly converting chemical energy into electrical energy with high efficiency and low emissions [1]. Anode, cathode, electrolyte, and interconnect wires are the basic components of SOFCs [1]. Researchers have investigated many different aspects of SOFCs, such as configurations [2,3], materials [4–8], component microstructures [9–12], electrochemical performance [11–14], and thermal stress [14–17]. Although these examples are representative of the research areas that have been investigated, they are by no means exhaustive. Researchers have also employed a variety of approaches to investigate problems

related to SOFCs: analytical [3], experimental [4–12], and computational [2,13–17].

Research has established that electrochemical performance of SOFCs is significantly affected by component microstructure [11,12]. In contrast, few studies have investigated the effects of microstructure on mechanical performance [16]. However, mechanical durability of the SOFC under steady-state and transient thermal loads is a significant aspect of performance; it is thus important to understand the effect of component microstructure on probability of failure under thermal loads.

In this work, we perform finite element analysis (FEA) of thermal stresses induced in reconstructed SOFC cathode microstructures under spatially uniform temperature fields. Three-dimensional finite element (FE) models of SOFC cathode microstructures are generated from a stack of two-dimensional microstructure images. The models are subjected to FEA to determine thermal stresses due to a steady-state temperature change from room temperature up to operating temperature. The calculated thermal stresses are analyzed using the Weibull method to

\* Corresponding author. Tel.: +1 860 486 2746; fax: +1 860 486 2298.

E-mail address: [jhkim@engr.uconn.edu](mailto:jhkim@engr.uconn.edu) (J.-H. Kim).

calculate the probability of failure. The cathode material is 50:50 wt.% LSM–YSZ. The effects of temperature-dependent material properties on the probability of failure of the cathode are investigated. A cathode model of 30:70 LSM:YSZ composition is derived using a heuristic scheme to investigate the effect of varying volume fractions on mechanical behavior under temperature loads.

Anode (50:50 wt.% NiO:YSZ) and cathode (50:50 wt.% LSM:YSZ) microstructures have previously been analyzed for thermal stress using finite elements by the authors [17]. This study extends the work by including detailed validation of the original and derived cathode microstructures, and by considering the effects of varying phase volume fractions on the mechanics of cathode microstructures under thermal stress. A simple heuristic scheme has been developed to derive cathode microstructures of varying compositions within a limited range from the original, real microstructures. Construction of such derived microstructures will provide physical insights on the effects of phase compositions on the mechanics of electrode structures in SOFC, which in reality possess varied compositions through the thickness direction to increase material compatibility between electrolyte and electrodes and to improve overall cell performance.

## 2. Image-based finite element microstructure models

### 2.1. Models based on original images

Three-dimensional (3-D) FE microstructure models were reconstructed from 41 two-dimensional (2-D) cross-sectional images of cathode microstructure. The 2-D images were obtained by Dr. Scott Barnett's research group at Northwestern University [9,10], using focused ion beam-scanning electron microscopy (FIB-SEM). Examples of the 2-D images are shown in Fig. 1. These images are of the real cathode microstructure having 50:50 LSM:YSZ composition.

In the SEM cathode images, white (pixel value = 255) represents LSM, gray (pixel value = 127) represents YSZ, and black (pixel value = 0) represents the pores. The original cathode image dimensions are 217 pixels (width)  $\times$  147 pixels (height). The  $x$ – $y$  (in-plane) spatial resolution between pixels is 40.8 nm and the  $z$ -spacing between images is 53.3 nm. The cathode images are thus of size 8.85  $\mu\text{m}$  (width)  $\times$  6.00  $\mu\text{m}$  (height).

Finite element modeling was carried out using the commercial FE software ABAQUS [18]. This was done by writing MATLAB® [19] programs to generate ABAQUS input files with all relevant data for running the FE analysis. The 3-D FE model was reconstructed from the 2-D images using 3-D finite elements (8-node brick elements). In order to increase computational efficiency for 3-D analysis using finite element method, we reduced the full model to a representative model in which we sacrifice some details of phase geometry but microstructural skeleton that is crucial to stress analysis remains almost unchanged. To provide validation data for this present approach, we used 2D cathode microstructure images and calculated three-phase boundary (TPB) density and phase surface area density for the original, full-size

50:50 wt.% LSM:YSZ cathode, as well as the reduced 50:50 cathode. The data agreed reasonably well with those reported in the literature [10,12]. This quantitative evidence may support the validity of the reduced model to a limited range which provides a basis for mechanical stress analysis that can achieve computational efficiency.

The original images of the cathode were first simplified by sampling pixels at regular intervals to reduce the image resolution while retaining a sufficiently detailed microstructure for the purposes of stress analysis. The simplified cathode images were 3.51  $\mu\text{m}$  (width)  $\times$  3.02  $\mu\text{m}$  (height) in size. The depth of the voxel was 53.3 nm. The next step in the model generation process was image stacking. A stack of all the 2-D ( $x$ – $y$  plane) images was created in the  $z$ -direction by using a cell array construct to arrange the images consecutively. An initially blank “buffer” plane (of the same size as each image) was then introduced between each pair of consecutive images. This was necessary to achieve a simple “step” variation in material properties between corresponding regions in two consecutive images. The gaps between consecutive images were filled by assigning one 8-node brick element to each voxel. Consider the  $n$ th and  $(n + 1)$ th images, and the buffer plane between them. The voxel connecting a given pixel on the  $n$ th image with the corresponding pixel location on the buffer plane was assigned to the element set corresponding to the value of the pixel on the  $n$ th image. Similarly, the voxel connecting a given pixel on the  $(n + 1)$ th image with the corresponding pixel location on the buffer plane was assigned to the element set corresponding to the value of the pixel on the  $(n + 1)$ th image. Thus, the geometry of the cathode microstructure was reconstructed in the 3-D FE models, with a step variation in material regions between consecutive images.

The volume fractions of phases in each 3-D model were calculated by counting the number of voxels corresponding to each phase (based on pixel value), and dividing by the total number of voxels in the model. Information concerning the material properties, boundary conditions, initial temperature, temperature field and required outputs (e.g. principal stresses) was also specified in the input file. The input file was then run using ABAQUS. Various free-body cuts of the 50:50 LSM:YSZ 3-D FE cathode model are shown in Fig. 2.

### 2.2. Derived model and validation

In order to study the effect of composition on the probability of failure of the cathode, we derived from the original images a 3-D model having volume fractions different than those of the original 50:50 LSM:YSZ model. The compositions of the models included in this study are given in Table 1 below.

A heuristic scheme was developed to derive the 3-D cathode model of 30:70 LSM:YSZ composition from the original 50:50 LSM:YSZ images. Boundary pixel modification was used to effect volume fraction alterations. This algorithm involved the identification of pixels initially lying on two- or three-phase boundaries in the original images, by comparison of pixel values with nearest in-

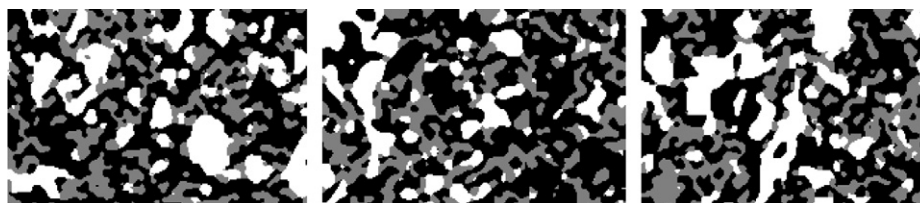


Fig. 1. Two-dimensional SEM images of typical cross-sections of original 50:50 wt.% LSM:YSZ cathode [10].

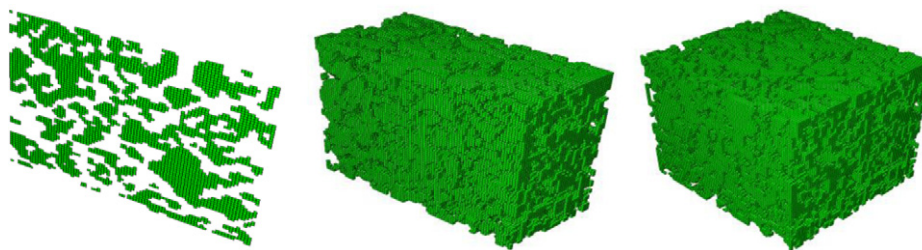


Fig. 2. Free-body cuts of the three-dimensional reduced-size FE cathode model.

plane neighbors. Boundary pixels were identified as black pixels at corresponding locations in a new (initially empty) cell array (the “boundary array”), while interior pixels were identified as white pixels in this new boundary array, which was of identical size as the original image stack. The locations of boundary pixels in the original image array were picked out from the boundary array by identifying black pixels in it. The values of pixels adjacent to boundary locations in the original image array were modified according to heuristic rules derived by trial-and-error, until the desired volume fractions of each phase were obtained in the corresponding 3-D model. The boundary pixel identification algorithm is illustrated in Fig. 3.

The steps in the heuristic algorithm are illustrated in Fig. 4, which shows how the algorithm operates in a step-by-step manner on cathode images from the 50:50 model to derive the 30:70 model by changing the relative proportions of pixels of different phases. The microstructural characteristics of the derived 30:70 cathode model were validated by calculating three-phase boundary (TPB) density and phase surface area densities from the stack of 2-D images, and comparing these values with data available in the literature (Tables 2 and 3). The TPB density and surface area density calculation algorithms were first validated by calculating the TPB and surface area densities for the full-size 50:50 cathode model, for which data are already available in the literature [10,12]. TPB length is calculated from the 2-D image stack using the boundary array described above, by identifying three-phase boundary points through pixel value comparison with nearest neighbors. TPB density ( $\mu\text{m}^{-2}$ ) is calculated by dividing the TPB length ( $\mu\text{m}$ ) by the total reconstructed volume of the corresponding model ( $\mu\text{m}^3$ ). The phase surface area is calculated from the boundary array by counting the total numbers of surface elements belonging to each phase. Finally, the surface area density ( $\mu\text{m}^{-1}$ ) of that phase is calculated by dividing the total surface area of the phase ( $\mu\text{m}^2$ ) by the total reconstructed volume of the model ( $\mu\text{m}^3$ ).

From Table 2, we can see that there is reasonable agreement between the TPB and surface area densities calculated by the algorithms for the full and reduced 50:50 cathode models, and those reported in the literature. For the reduced 30:70 cathode model derived from the original images, the calculated surface area densities are in closer agreement with the literature than the calculated TPB density. This is probably due to the fact that the TPB density calculation algorithm makes use of the 2-D images, while

the values reported in [12] are based on detailed analysis of the 3-D microstructure data set and on an analytical model [20]. It is worth noting here that Vivet et al. [21] have reported TPB densities as high as  $7.2\text{--}11.2 \mu\text{m}^{-2}$  for Ni-YSZ anode cermet samples having NiO wt.% values varying from 45% to 61%, with sample volumes varying from  $349.39$  to  $957.95 \mu\text{m}^3$ . Moreover, Wilson et al. [12] have pointed out that TPB density may be higher for cathodes than for anodes due to the finer cathode microstructures. In this regard, the TPB density of  $12.9 \mu\text{m}^{-2}$  obtained for the reduced 30:70 cathode model may be considered reasonable, given that the reconstructed volume for the reduced cathode is  $45.2 \mu\text{m}^3$  (Table 3).

### 3. Finite element thermal stress analysis

#### 3.1. Study design

Finite element analyses of the cathode microstructure models were carried out to investigate thermal stresses due to various temperature fields. The effects of varying phase volume fractions and temperature-dependent material properties on thermal stresses and probability of failure were investigated. The FE analyses were divided into different categories as explained in Table 4. In each case, the FE model was subjected to fixed boundary conditions (i.e. all nodes on each of the six faces were allowed neither to translate nor to rotate). The behavior of the model with increasing temperature loads was investigated by subjecting the model to eight different spatially uniform predefined temperature fields of magnitude  $120^\circ\text{C}$ ,  $220^\circ\text{C}$ ,  $320^\circ\text{C}$ , ...,  $820^\circ\text{C}$ . In each analysis, the initial temperature was specified as  $20^\circ\text{C}$  (room temperature), so that the model was subjected to eight different magnitudes of temperature change ( $\Delta T = 100^\circ\text{C}$ ,  $200^\circ\text{C}$ ,  $300^\circ\text{C}$ , ...,  $800^\circ\text{C}$ ).

#### 3.2. Material properties

Table 5 lists the room temperature material properties used for YSZ and LSM.

Fig. 5 shows the variation of the CTE of YSZ with temperature [22] and the variation of the Young's modulus of LSM and YSZ with temperature [4]. The CTE of LSM was assumed constant over the temperature range considered. The room temperature value of the CTE of LSM (Table 5) was used in the FE analyses.

#### 3.3. Stress analysis

The 3-D FE model of the cathode (50:50 LSM:YSZ) is shown in Fig. 6. The model has 244584 elements and 395131 nodes. The von Mises stress contour plots for the 50:50 LSM:YSZ cathode for  $\Delta T = 100^\circ\text{C}$  and  $800^\circ\text{C}$  are shown considering temperature-dependent material properties in Fig. 7. The stress values are in units of  $\text{N m}^{-2}$ , i.e. Pa.

**Table 1**  
Original (50:50) and derived (30:70) LSM:YSZ compositions of cathode [12].

Cathode model designation	Composition (weight percentage) LSM:YSZ	Volume fraction of LSM (%)	Volume fraction of YSZ (%)	Volume fraction of pores (%)
Cathode 5050	50:50	23.56	24.48	51.96
Cathode 3070	30:70	15.81	37.39	46.80

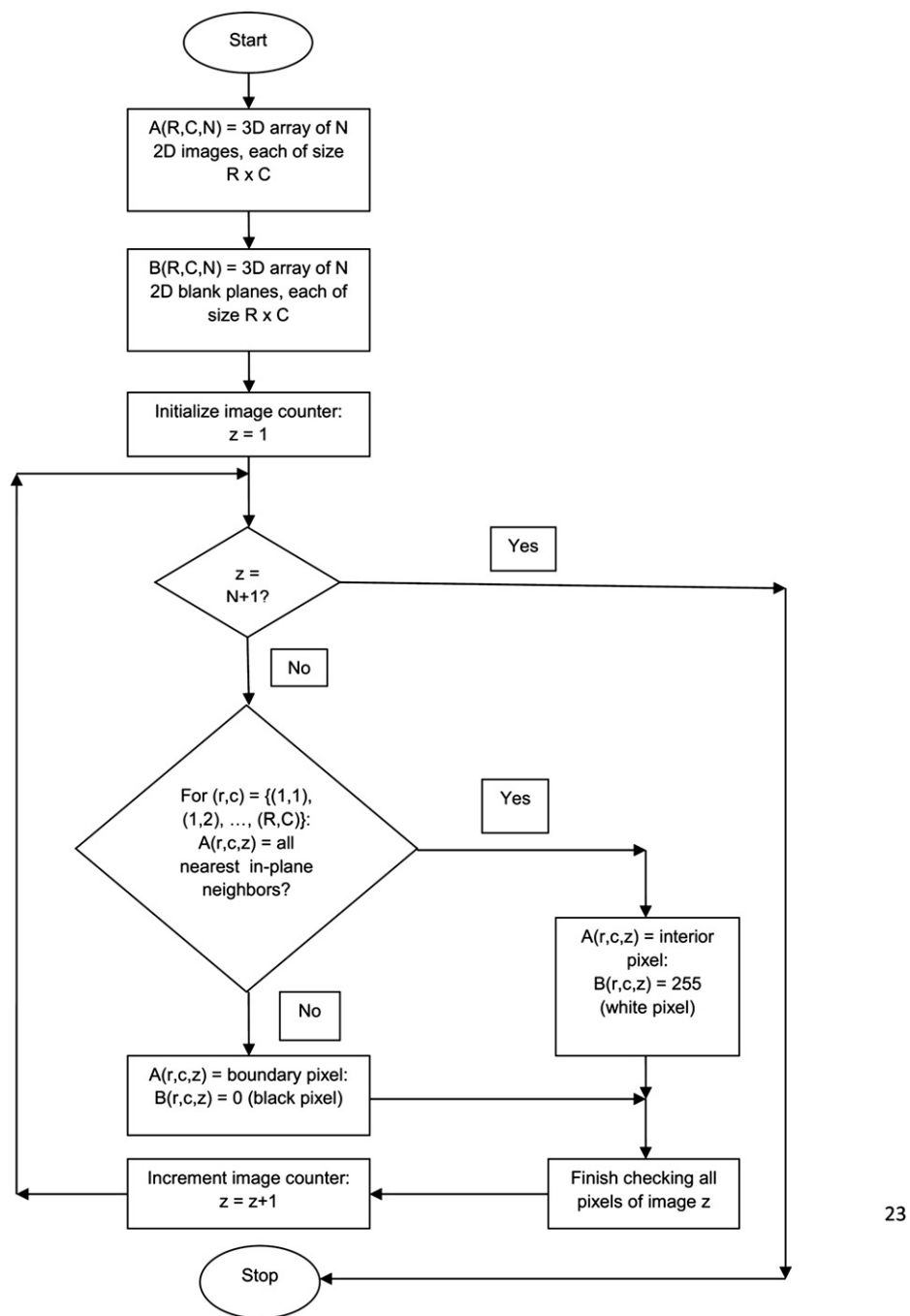


Fig. 3. Algorithm for boundary pixel detection.

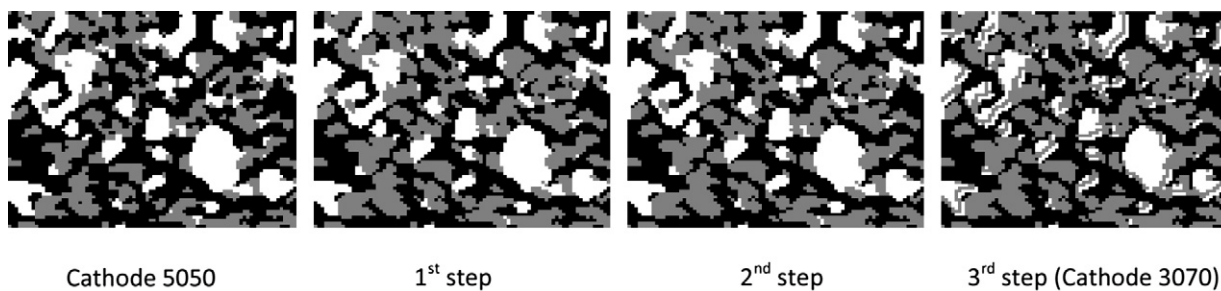


Fig. 4. Boundary pixel modification heuristic operating on original image of 50:50 LSM:YSZ cathode.

**Table 2**

Full and reduced cathode models.

Model size and wt.% LSM:YSZ	TPB density from algorithm ( $\mu\text{m}^{-2}$ )	TPB density from literature ( $\mu\text{m}^{-2}$ )	LSM SA density from algorithm ( $\mu\text{m}^{-1}$ )	LSM SA density from literature ( $\mu\text{m}^{-1}$ )	YSZ SA density from algorithm ( $\mu\text{m}^{-1}$ )	YSZ SA density from literature ( $\mu\text{m}^{-1}$ )	Pore SA density from algorithm ( $\mu\text{m}^{-1}$ )	Pore SA density from literature ( $\mu\text{m}^{-1}$ )
Full, 50:50	5.74	7.35 [10]	1.83	1.80 [12]	3.08	3.00 [12]	4.05	3.90 [12]
Reduced, 50:50	8.40	7.35 [10]	1.67	1.80 [12]	2.57	3.00 [12]	3.83	3.90 [12]
Reduced, 30:70	12.9	6–9 [12]	1.48	1.30 [12]	3.68	4.39 [12]	3.79	4.70 [12]

SA = Surface area.

**Table 3**

Full and reduced volumes of cathode models.

Model	X–Y pixel resolution (nm)	Z-resolution (spacing between images) (nm)	Height (pixels $\mu\text{m}^{-1}$ )	Width (pixels $\mu\text{m}^{-1}$ )	Number of images used	Volume of model ( $\mu\text{m}^3$ )
Full	40.8	53.3	147/6.00	217/8.85	242	682
Reduced	40.8	53.3	74/3.02	86/3.51	41	45.2

Fig. 7 shows that as  $\Delta T$  increases from 100 °C to 800 °C, the stresses in the cathode also increase. Thermal stress is proportional to the CTE and  $\Delta T$ , and the CTE of YSZ increases with temperature while the CTE of LSM is assumed constant over the temperature range considered. Also, the stress contours show that the stresses are greater near the pores due to stress concentration. Similar results were obtained for the case with temperature-independent material properties. The cathode model with 30:70 LSM:YSZ composition shows similar behavior in both cases. The effects of temperature-independent versus temperature-dependent material properties on the principal tensile stresses induced in the cathode are discussed in conjunction with probability of failure estimation, where the effects of varying phase compositions on thermal stresses and probability of failure are also discussed.

#### 4. Failure probability estimation using the Weibull method

Ceramic materials exhibit brittle behavior under tensile stress. Also, unlike metals, they show wide variability in tensile strength values and follow a statistical strength distribution. Thus, the Weibull method of analysis [2,23], was used to calculate the probability of failure of the SOFC cathode.

According to the Weibull method, the survival probability of a particular component  $j$  under the action of a tensile stress  $\sigma$  is given by [2]:

$$P_s^j(\sigma, V_j) = \exp\left(-\int_{V_j} \left(\frac{\sigma}{\sigma_0}\right)^m \frac{dV_j}{V_0}\right)$$

Here  $j$  = cathode,  $V_j$  is the volume of component  $j$ ,  $V_0$  is a characteristic specimen volume (reference volume) for the material of component  $j$ ,  $\sigma_0$  is the characteristic strength of the material of component  $j$ , and  $m$  is the Weibull modulus of the material. The characteristic strength  $\sigma_0$  is also the scale parameter for the

**Table 4**

Finite element analyses of cathode.

Case	LSM	YSZ	Temperature -dependence (LSM)	Temperature -dependence (YSZ)
Temperature -independent	Linear elastic	Linear elastic	None	None
Temperature -dependent	Linear elastic	Linear elastic	Young's modulus	Young's modulus, CTE

distribution, while the Weibull modulus  $m$  is the shape parameter. The reference volume  $V_0$  is related to the characteristic strength  $\sigma_0$  of the material. In this study, the Weibull method was modified to account for the fact that the cathode material is a composite made up of two different components (LSM and YSZ). The Weibull parameters used for the ceramic materials (LSM and YSZ) are shown in Table 6. Room temperature values of the Weibull parameters were used in this study.

The results of each stress analysis were post-processed by writing programs to extract the three principal stress values from each ceramic (LSM/YSZ) element in the cathode models. These principal stresses were then used to perform a Weibull analysis to determine the probability of failure of the cathode at each  $\Delta T$  value. Since the SOFC component materials are subjected to a multi-axial state of stress, the total survival probability of each ceramic phase of the cathode under the action of the three principal stresses ( $\sigma_1$ ,  $\sigma_2$ , and  $\sigma_3$ ) was calculated. The principal stresses were assumed to act independently, and the total survival probability was calculated as the product of the survival probabilities under the action of each individual principal stress [2]:

$$P_s^j(\bar{\sigma}, V_j) = \prod_{i=1}^3 P_s^j(\sigma_i, V_j)$$

Also,

$$P_s^j(\sigma_i, V_j) = \exp\left(-\int_{V_j} \left(\frac{\sigma_i}{\sigma_0}\right)^m \frac{dV_j}{V_0}\right)$$

Here,  $j$  = LSM or YSZ for the cathode, and  $i = 1, 2$ , and 3. Only tensile values of the three principal stresses were used in the Weibull analysis. The probability of failure of each phase was then calculated as follows [15]:

$$P_f = 1.0 - P_s^j(\bar{\sigma}, V_j)$$

**Table 5**

Room temperature material properties used in FE analyses [15].

Material	Young's modulus (GPa)	Poisson's ratio	CTE ( $10^{-6} \text{ } ^\circ\text{C}^{-1}$ )
YSZ	205	0.30	10.40
LSM	40	0.25	11.40



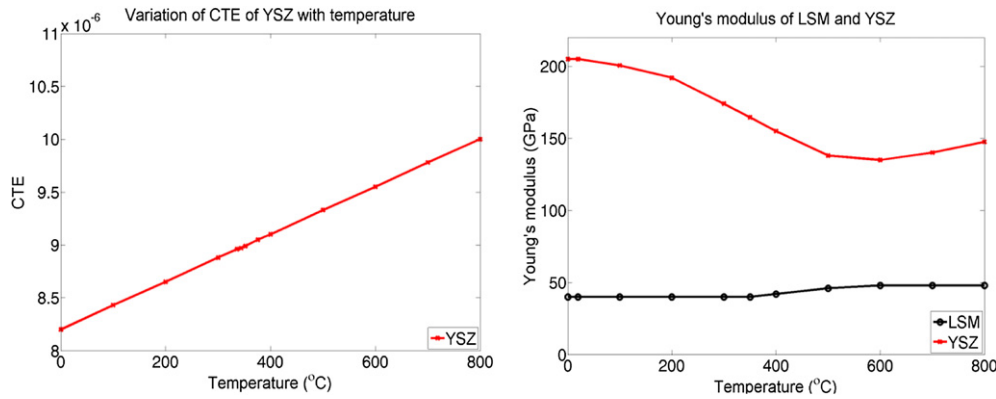


Fig. 5. (left) Variation of CTE of YSZ with temperature; (right) variation of Young's modulus of LSM and YSZ with temperature.

#### 4.1. Probability of failure analyses

Since the cathode is composed of two different ceramic materials (LSM–YSZ), the probability of failure of the cathode was calculated by extracting positive (tensile) values of the three principal stresses from each element in the LSM and YSZ element sets of the cathode FE model, and subjecting these to Weibull analyses. This resulted in two different probability of failure values for the LSM and YSZ phases of the cathode, which were combined into a single probability of failure value for the cathode by assuming that the cathode fails when either phase fails (or when both phases fail simultaneously). The probability that both phases fail simultaneously was calculated by assuming that the failures of the two phases are independent events, and hence the probability of simultaneous failure of the two phases is the product of the probabilities of failure of LSM and YSZ:

$$P_f^{\text{cathode}} = P_f(\text{LSM or YSZ}) = P_f(\text{LSM} \cup \text{YSZ})$$

$$\Rightarrow P_f^{\text{cathode}} = P_f(\text{LSM}) + P_f(\text{YSZ}) - P_f(\text{LSM} \cap \text{YSZ})$$

$$\Rightarrow P_f^{\text{cathode}} = P_f(\text{LSM}) + P_f(\text{YSZ}) - P_f(\text{LSM})P_f(\text{YSZ})$$

The probability of failure ( $P_f$ ) values for the LSM and YSZ phases of each cathode model were calculated and combined, as described above, at each  $\Delta T$  value (100  $^{\circ}\text{C}$ , 200  $^{\circ}\text{C}$ , ..., 800  $^{\circ}\text{C}$ ) for both the cases described in Table 4 (temperature-independent material properties and temperature-dependent material properties). These values are plotted in Fig. 8.

The  $P_f$  plots for both cathode models show that the probability of failure of the cathode increases with increasing  $\Delta T$  values (and hence increasing stresses), for both temperature-independent and

temperature-dependent material properties, as expected. These values may be verified against the cathode  $P_f$  values reported by Anandakumar et al. [15]. They investigated the probability of failure of functionally graded SOFCs subjected to spatially uniform thermal loading. Although the microstructures of the SOFC electrodes have not been considered in [15], the  $P_f$  values reported in that work have been calculated using the Weibull method, with the same Weibull parameter values as used in the present study. Anandakumar et al. [15] have reported (cf. Figure 16 in their paper)  $P_f$  values varying in average  $10^{-12}$  to  $10^{-5}$  for graded and layered LSM cathodes. The cathode  $P_f$  values in the present study vary between  $4.6 \times 10^{-13}$  and  $4.4 \times 10^{-6}$ , which is in good agreement with those reported in [15].

##### 4.1.1. Effects of temperature-dependent material properties

As seen from Fig. 8, higher  $P_f$  values are obtained when temperature-independent material properties (indicated by the solid lines) are considered, for both cathode models. A physical explanation for this observation is suggested by the temperature variation of the Young's modulus of YSZ. For YSZ,  $E$  decreases from a value of 205 GPa at  $T = 20^{\circ}\text{C}$  to a value of 147.5 GPa at 800  $^{\circ}\text{C}$ , as shown in Fig. 5. On the other hand, when temperature-independent material properties are considered, the Young's modulus of YSZ has a constant value of 205 GPa. This large decrease in the Young's modulus of YSZ with increasing temperature leads to lower stresses in the cathode with temperature-dependent material properties than with temperature-independent material properties. This in turn leads to lower  $P_f$  values with temperature-dependent material properties than with temperature-independent material properties. This is confirmed by the MPTS plot for the 50:50 cathode model shown in Fig. 9, which compares the maximum principal tensile stress induced in the YSZ and LSM phases of the model for temperature-independent and temperature-dependent material properties.

Fig. 9 shows that the MPTS induced in the LSM phase for temperature-dependent material properties is lower than the MPTS in the LSM phase for temperature-independent material properties over the entire temperature range. Similarly, the MPTS induced in the YSZ phase for temperature-dependent material properties is lower than the MPTS induced in the YSZ phase for temperature-independent material properties over the entire temperature range. This implies that the cathode  $P_f$  values, which are calculated on the basis of the tensile principal stresses in the LSM and YSZ phases, will be lower with temperature-dependent material properties than with temperature-independent material properties.

##### 4.1.2. Effects of variation of phase volume fractions

Fig. 8 shows the  $P_f$  values for the two cathode models for temperature-independent and temperature-dependent material properties. For temperature-independent material properties, the

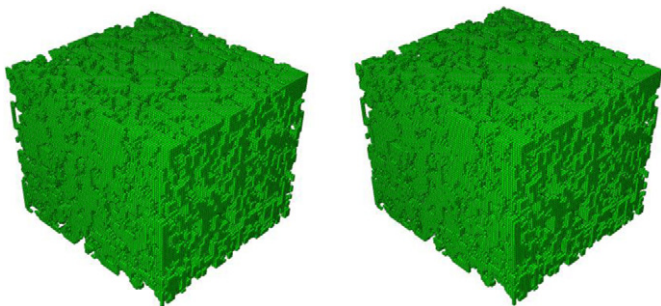
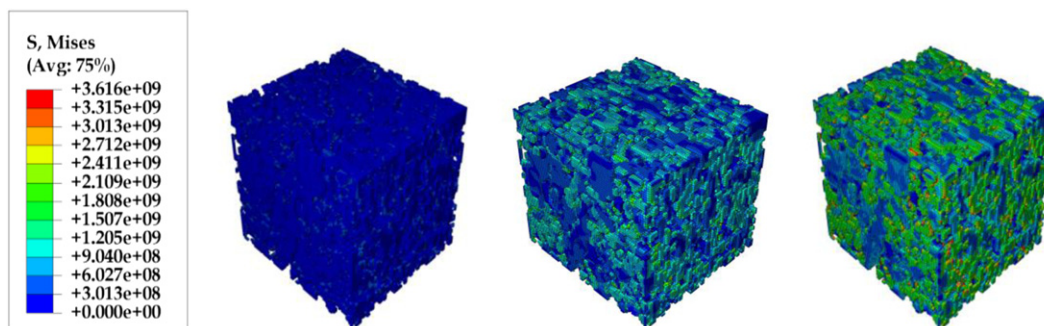


Fig. 6. Three-dimensional reduced-size FE models of 50:50 (left) and 30:70 (right) wt.% LSM:YSZ cathode.



**Fig. 7.** Von Mises stress contour plots (in Pa) for 50:50 LSM:YSZ cathode considering temperature-dependent material properties:  $\Delta T = 100$  °C (left),  $\Delta T = 500$  °C (middle),  $\Delta T = 800$  °C (right).

**Table 6**  
Weibull parameters of ceramic materials (room temperature values) [2].

Material	Weibull modulus, $m$	Characteristic strength, $\sigma_0$ (MPa)	Reference volume, $V_0$ (mm <sup>3</sup> )
LSM	7.0	52.0	1.21
YSZ	7.0	446.0	0.35

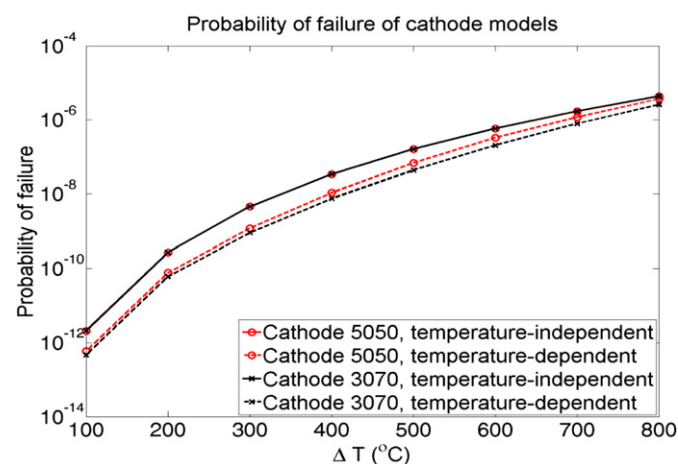


**Fig. 8.** Probability of failure of cathode models.

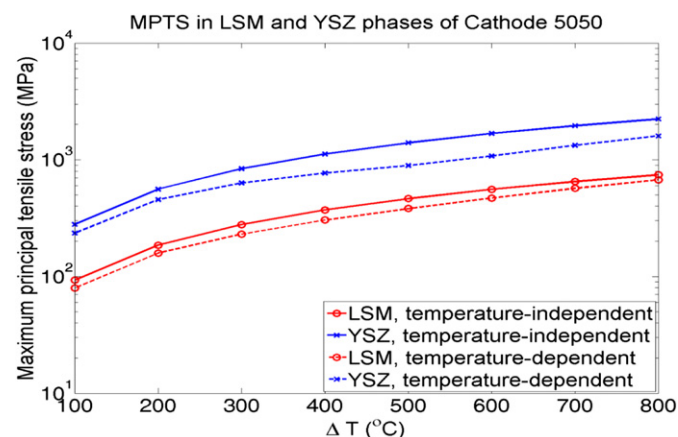


**Fig. 9.** Maximum principal tensile stress in LSM and YSZ phases of 50:50 LSM:YSZ cathode model.

models show almost identical  $P_f$  values over the entire temperature range, as indicated by the two solid lines that coincide with one another. This indicates that given temperature-independent material properties and similar pore volume fractions (51.96% for the 50:50 LSM:YSZ model and 46.80% for the 30:70 LSM:YSZ model), the variation in the composition of the model (in terms of volume fractions of LSM and YSZ) has very little effect on the  $P_f$  values. However, Fig. 8 shows that when temperature-dependent material properties are considered, the volume fraction of YSZ plays a significant role in determining the  $P_f$  values, since the Young's modulus of YSZ undergoes a large decrease with increasing temperature. Based on the previous discussion, we may anticipate that lower stresses will be induced in the 30:70 model, since it has a higher volume fraction of YSZ than the 50:50 model. These results are indeed observed in Fig. 8. The 30:70 LSM:YSZ model shows lower  $P_f$  values than the 50:50 model, for temperature-dependent material properties, in Fig. 8.

## 5. Concluding remarks

This paper addresses finite element thermal stress analysis of microstructure-based SOFC cathode models. It investigates the effects of temperature-dependent material properties and varying phase volume fractions of cathode materials on the behavior of the cathode model under temperature loads. In this paper, an approximate heuristic scheme has been used, based on boundary pixel manipulation of original 50:50 wt.% LSM:YSZ microstructure images, to derive a microstructure of 30:70 wt.% LSM:YSZ composition. Construction of derived microstructures using such heuristic schemes may provide a simplified, approximate approach for investigating the effects of phase compositions on the mechanics of electrode structures, and is not intended to replace more rigorous approaches such as the random packing model. The critical findings are described as follows. First, consideration of temperature-independent material properties of the SOFC cathode materials results in higher probability of failure values than those obtained with temperature-dependent material properties. Second, the two cathode models studied, with similar pore volume fractions, showed the following trends. With temperature-independent material properties, limited variations in the volume fractions of LSM and YSZ phases had negligible effect on failure probability. With temperature-dependent material properties, the cathode model with higher volume fraction of YSZ was found to have lower stresses and lower probability of failure, due to the decrease in the Young's modulus of YSZ with increasing temperature.

The probability of failure of cathode  $P_f$  values in the present study vary between  $4.6 \times 10^{-13}$  and  $4.4 \times 10^{-6}$ , which is in good agreement with those reported in [15] varying in average  $10^{-12}$  to  $10^{-5}$  for

graded and layered LSM cathodes. The present work did not consider the effects of residual stresses, which can be an interesting topic in the future.

### Acknowledgments

The financial support for this work from the National Science Foundation under the Faculty Early Career Development (CAREER) Grant CMMI-0546225 (Material Design & Surface Engineering Program) is gratefully acknowledged. We also acknowledge the assistance from the research group of Dr. Scott Barnett at the Department of Materials Science and Engineering at Northwestern University, Evanston, Illinois. They shared their research findings, in the form of the 2-D SEM images of the cathode microstructure. We would also like to thank the anonymous reviewers for their insightful comments, which helped us improve our manuscript.

### References

- [1] S.C. Singhal, K. Kendall (Eds.), *High Temperature Solid Oxide Fuel Cells: Fundamentals, Design and Applications*, Elsevier Ltd., Oxford, 2003.
- [2] J. Laurencin, G. Delette, F. Lefebvre-Joud, M. Dupeux, A numerical tool to estimate SOFC mechanical degradation: case of the planar cell configuration, *Journal of the European Ceramic Society* 28 (2008) 1857–1869.
- [3] T. Zhang, Q. Zhu, W.L. Huang, Z. Xie, X. Xin, Stress field and failure probability analysis for the single cell of planar solid oxide fuel cells, *Journal of Power Sources* 182 (2008) 540–545.
- [4] S. Giraud, J. Canel, Young's modulus of some SOFCs materials as a function of temperature, *Journal of the European Ceramic Society* 28 (2008) 77–83.
- [5] A. Selcuk, A. Atkinson, Strength and toughness of tape-cast yttria-stabilized zirconia, *Journal of the American Ceramic Society* 83 (8) (2000) 2029–2035.
- [6] H. Toftegaard, B.F. Sorensen, S. Linderroth, M. Lundberg, S. Feih, Effects of heat-treatments on the mechanical strength of coated YSZ: an experimental assessment, *Journal of the American Ceramic Society* 92 (11) (2009) 2704–2712.
- [7] A. Selcuk, A. Atkinson, Elastic properties of ceramic oxides used in solid oxide fuel cells (SOFC), *Journal of the European Ceramic Society* 17 (1997) 1523–1532.
- [8] M. Pihlatie, A. Kaiser, M. Mogensen, Mechanical properties of NiO/Ni-YSZ composites depending on temperature, porosity and redox cycling, *Journal of the European Ceramic Society* 29 (2009) 1657–1664.
- [9] J.R. Wilson, W. Kobsiriphat, R. Mendoza, H.-Y. Chen, J.M. Hiller, D.J. Miller, K. Thornton, P.W. Voorhees, S.B. Adler, S.A. Barnett, Three-dimensional reconstruction of a solid-oxide fuel-cell anode, *Nature Materials* 5 (2006) 541–544.
- [10] J.R. Wilson, A.T. Duong, M. Gameiro, H.-Y. Chen, K. Thornton, D.R. Mumm, S.A. Barnett, Quantitative three-dimensional microstructure of a solid oxide fuel cell cathode, *Electrochemistry Communications* 11 (2009) 1052–1056.
- [11] J.R. Wilson, S.A. Barnett, Solid oxide fuel cell Ni-YSZ anodes: effect of composition on microstructure and performance, *Electrochemical and Solid State Letters* 11 (10) (2008) B181–B185.
- [12] J.R. Wilson, J.S. Cronin, A.T. Duong, S. Rukes, H.-Y. Chen, K. Thornton, D.R. Mumm, S. Barnett, Effect of composition of  $(\text{La}_{0.8}\text{Sr}_{0.2}\text{MnO}_3\text{--Y}_2\text{O}_3\text{--stabilized ZrO}_2)$  cathodes: correlating three-dimensional microstructure and polarization resistance, *Journal of Power Sources* 195 (2010) 1829–1840.
- [13] G.M. Goldin, H. Zhu, R.J. Kee, D. Bierschen, S.A. Barnett, Multidimensional flow, thermal, and chemical behavior in solid-oxide fuel cell button cells, *Journal of Power Sources* 187 (2009) 123–135.
- [14] A. Selimovic, M. Kemm, T. Torisson, M. Assadi, Steady state and transient thermal stress analysis in planar solid oxide fuel cells, *Journal of Power Sources* 145 (2005) 463–469.
- [15] G. Anandakumar, N. Li, A. Verma, P. Singh, J.-H. Kim, Thermal stress and probability of failure analyses of functionally graded solid oxide fuel cells, *Journal of Power Sources* 195 (2010) 6659–6670.
- [16] R. Clague, P.R. Shearing, P.D. Lee, Z. Zhang, D.J.L. Brett, A.J. Marquis, N.P. Brandon, Stress analysis of solid oxide fuel cell anode microstructure reconstructed from focused ion beam tomography, *Journal of Power Sources* 196 (2011) 9018–9021.
- [17] S. Vaidya, J.-H. Kim, Continuum mechanics of solid oxide fuel cells using three-dimensional reconstructed microstructures, in: Y.X. Gan (Ed.), *Continuum Mechanics—Progress in Fundamentals and Engineering Applications*, InTech, Rijeka, 2012, pp. 73–88.
- [18] Abaqus v6.9, Dassault Systemes Simulia Corp., Providence, Rhode Island.
- [19] MATLAB ®R2010a, The MathWorks, Inc., Natick, Massachusetts.
- [20] W. Zhu, D. Ding, C. Xia, Enhancement in three-phase boundary of SOFC electrodes by an ion impregnation method: a modeling comparison, *Electrochemical and Solid-State Letters* 11 (2008) B83–B86.
- [21] N. Vivet, S. Chupin, E. Estrade, A. Richard, S. Bonnamy, D. Rochais, E. Bruneton, Effect of Ni content in SOFC Ni-YSZ cermet: a three-dimensional study by FIB-SEM tomography, *Journal of Power Sources* 196 (2011) 9989–9997.
- [22] J. Johnson, J. Qu, Effective modulus and coefficient of thermal expansion of Ni-YSZ porous cermet, *Journal of Power Sources* 181 (2008) 85–92.
- [23] W. Weibull, A statistical distribution function of wide applicability, *Journal of Applied Mechanics* 18 (1951) 293–297.